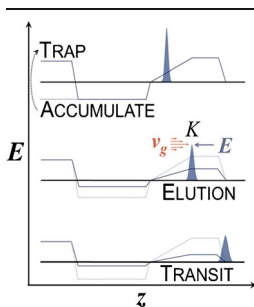


Fundamentals of Trapped Ion Mobility Spectrometry

Karsten Michelmann, Joshua A. Silveira, Mark E. Ridgeway, Melvin A. Park

Bruker Daltonics, 40 Manning Road, Billerica, MA 01821, USA



Abstract. Trapped ion mobility spectrometry (TIMS) is a relatively new gas-phase separation method that has been coupled to quadrupole orthogonal acceleration time-of-flight mass spectrometry. The TIMS analyzer is a segmented rf ion guide wherein ions are mobility-analyzed using an electric field that holds ions stationary against a moving gas, unlike conventional drift tube ion mobility spectrometry where the gas is stationary. Ions are initially trapped, and subsequently eluted from the TIMS analyzer over time according to their mobility (K). Though TIMS has achieved a high level of performance ($R > 250$) in a small device (< 5 cm) using modest operating potentials (< 300 V), a proper theory has yet to be produced. Here, we develop a quantitative theory for TIMS via mathematical derivation and simulations. A one-

dimensional analytical model, used to predict the transit time and theoretical resolving power, is described. Theoretical trends are in agreement with experimental measurements performed as a function of K , pressure, and the axial electric field scan rate. The linear dependence of the transit time with $1/K$ provides a fundamental basis for determination of reduced mobility or collision cross section values by calibration. The quantitative description of TIMS provides an operational understanding of the analyzer, outlines the current performance capabilities, and provides insight into future avenues for improvement.

Keywords: Ion mobility spectrometry, TIMS theory

Received: 1 July 2014/Revised: 4 September 2014/Accepted: 4 September 2014/Published online: 21 October 2014

Introduction

Ion mobility spectrometry (IMS) involves the separation and characterization of gas-phase ions based upon their transport properties through a buffer gas in the presence of an electric field. Conventional IMS technology emerged from early drift tube IMS experiments wherein a constant axial electric field, E , forces ions through a gas at a drift velocity, v_d , given by [1, 2]

$$v_d = K E \quad (1)$$

where K is the ion mobility coefficient. Whereas drift tube IMS pushes ions through a stationary gas, another early IMS approach by Zeleny held ions of a particular mobility stationary against a counter-current of gas flow [3]; unfortunately, after an initial set of experiments, this approach was essentially abandoned for decades. In recent years, however, an analogous

approach was employed by Huang and Ivory for liquid phase ion mobility experiments (*viz.*, capillary electrophoresis) in a technique termed “electric field gradient focusing” (EFGF) [4]. EFGF employs an electric field that holds ions stationary against a moving fluid. The electric field strength varies as a function of position along the separation axis creating a correlation between an ion’s mobility coefficient and its equilibrium position along the length of the capillary. The work of Huang and Ivory represents the liquid phase equivalent of trapped IMS (TIMS) and inspired the theory presented below.

Similarly, Loboda demonstrated gas-phase IMS in a segmented quadrupole ion guide using a counter-flow of gas and an axial electric field that was progressively increased to induce mobility-dependent elution from the analyzer [5]. Though the segmented quadrupole approach displayed superior analytical figures-of-merit compared with drift tube IMS of comparable geometric length, resolving power ($R \leq 40$) was ultimately limited by the low operational pressure (~ 50 mTorr) and corresponding low axial electric fields.

Meanwhile, hybridization of low pressure (~ 0.5 to 10 Torr) drift tube IMS with mass spectrometry (MS) has proven to be valuable for a number of chemical [6–10], physical [11–15], and biological [16–31] applications. However, radial diffusion of the ion swarm during transit through the drift tube presents a significant limitation, since the diffusion coefficient is

Electronic supplementary material The online version of this article (doi:10.1007/s13361-014-0999-4) contains supplementary material, which is available to authorized users.

Correspondence to: Melvin Park; e-mail: map@bdal.com

inversely proportional to pressure. Several approaches have been employed to overcome this principal limitation including reducing the drift gas temperature [32–34], radial confinement of the ion swarm during IMS separation [35–38], and implementation of ion funnels [39–46]. Interestingly, during development of the electrodynamic ion funnel for MS applications, Smith et al. noted that unwanted background species of high K could be removed from the ion beam by applying an adjustable potential to the conductance limiting aperture at the exit of the device [47]. In an analogous experiment, Baykut et al. showed that the voltage required to attenuate an ion signal could be directly correlated to K [48].

Recently introduced by Park et al., TIMS technology builds upon the aforementioned experimental approaches, yielding a versatile device with several attractive features including (1) the ability to operate in either MS or IM-MS mode with high ion transmission, (2) a relatively long but adjustable separation timescale (~ 10 ms to 1 s), (3) a compact design enabling efficient integration with MS, (4) the flexibility to adjust the duty cycle and resolving power in accordance with a particular analytical challenge, (5) the ability to determine reduced mobility or collision cross section values by straightforward calibration [49, 50], and (6) R that can exceed 250 [50], providing high IM-MS peak capacity and the ability to separate species having small differences in K .

In TIMS experiments, ions are initially trapped using radially-confining rf voltages and an axial electric field that counteracts the drag force exerted from a flow of gas [49, 51–53]. Ions are subsequently eluted from the analyzer as the magnitude of the axial electric field is progressively decreased. Though several promising analytical figures-of-merit have been demonstrated, the gas-phase ion dynamics have only been qualitatively described [49]. In the present work, TIMS fundamentals are comprehensively discussed by comparison of experimental data and simulations to a first-principles analytical model. The quantitative description clarifies the relationship between ion characteristics, instrument properties, and user-defined experimental parameters on the separation performance, and also provides a fundamental basis for current and future TIMS technology development.

Experimental

Instrumentation

A schematic representation of the TIMS device, its operation, and the coordinate system referred to herein is shown in Figure 1a and b. For IM-MS experiments, the TIMS funnel was incorporated into the first vacuum stage of a prototype maXis ESI-QqTOF (Bruker Daltonics, Billerica, MA, USA) mass spectrometer. As depicted in Figure 1a, the TIMS analyzer is comprised of a set of electrodes that form three regions: the entrance funnel, TIMS tunnel, and exit funnel. Note that in the entrance and exit funnel regions, the electrodes are spaced apart from one another to allow gas to flow freely between the plates; however, in the tunnel region, the gaps between adjacent plates

are eliminated such that gas is forced to flow through the tunnel. Both gas and ions are introduced to the TIMS funnel through the capillary. During operation, ions are deflected into the entrance funnel, whereas the gas may be pumped through a port opposite the capillary exit. Alternatively, all or part of the gas can be forced to flow through the TIMS tunnel where it is subsequently pumped away through a secondary port in the exit funnel region. In this work, the entrance and exit funnel regions are pumped using a Roots-type multistage dry vacuum pump (1670 L/min, Ebara, EV-SA20-2; Tokyo, Japan).

Each of the plates comprising the TIMS analyzer is segmented into quadrants to allow the application of independent potentials to each quadrant [54, 55]. An rf voltage (850 kHz, $230 V_{p-p}$) is applied to the quadrants of each of the plates to generate a radially confining pseudopotential. The rf potentials are applied such that a dipole field is produced in the entrance and exit funnels, whereas a quadrupole field is produced in the tunnel. The dipole field in the entrance and exit funnels is ideal for capturing and focusing ions into the tunnel and exit aperture (2 mm diameter), respectively, whereas the quadrupole field in the tunnel is ideal for radially confining ions near the tunnel axis during TIMS analysis (see Figure 1c). Division of the funnel plates into quadrants allows for a smooth transition from a dipole to a quadrupole and back to a dipole field as ions progress from the entrance funnel, into the tunnel, and through the exit funnel, respectively. Importantly, the radially confining rf quadrupole field in the TIMS tunnel has essentially no axial component and, therefore, does not interfere with the IMS measurement.

To create an axial electric field gradient (EFG), DC potentials are superimposed on each of the funnel and tunnel plates. The DC potentials in the tunnel and the accompanying EFG profile are set via a resistor divider. The resistor divider is comprised of a series of resistors positioned between adjacent plates along the length of the tunnel. The value of a given resistor is chosen so as to set the relative magnitude of the EFG at the position of its corresponding plates. Thus, the resistor values vary linearly with position in the region corresponding to the rising edge and have a single higher value in the region corresponding to the plateau (see Figure 1a and b). The profile of the EFG is set by the resistors, whereas potentials applied at either end of the resistor chain set the polarity and magnitude of the profile. Typically, a fixed DC potential is applied at the exit end of tunnel, whereas a scanned voltage is applied at the entrance of the tunnel to perform the TIMS analysis. It is, therefore, the magnitude and the rate of change of the entrance potential that is of principle interest when adjusting the mobility range, resolving power, and analysis speed. Because the overall “shape” of the EFG profile is fixed, the field strength on the plateau of the EFG, E_p , is proportional to the potential applied across the tunnel. That is, scanning the potential at the entrance of the tunnel in a linear manner scans the field strength at the plateau in a linear manner.

In the entrance and exit funnels, the DC electric field simply pushes ions downstream. However, in the TIMS tunnel, the DC

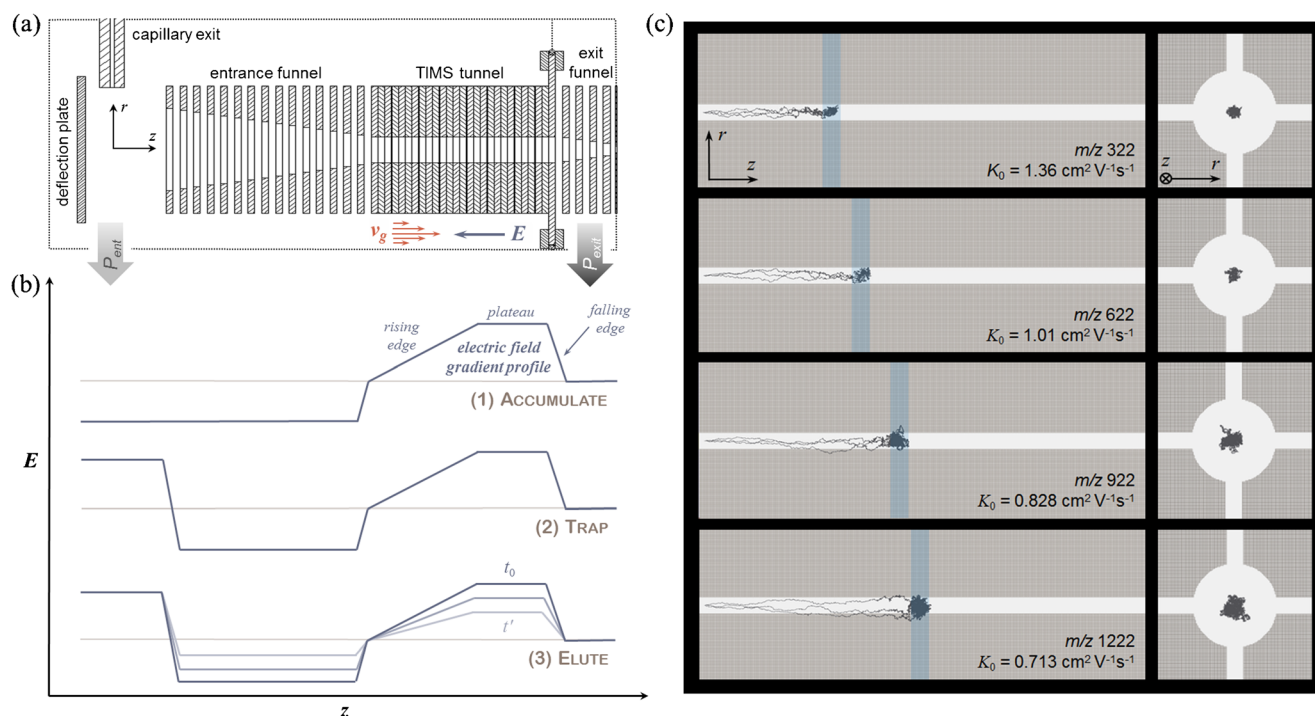


Figure 1. Schematic representation of TIMS components and general principles of operation. (a) Diagram of the TIMS tunnel including the orthogonal capillary ion inlet, deflection plate, entrance funnel, tunnel, and exit funnel. (b) Experimental analysis sequence shown, including plots of electric field strength, with respect to axial position. (c) SIMION simulations of the tunnel demonstrating the position-dependent trapping of select ESI tuning mix ions (left panel). Ions enter on the left side and their trajectories can be traced to their equilibrium position where they are trapped along the rising edge of the EFG profile. In the right panel, ion trajectories are viewed down the axis of the tunnel. A gas velocity of 90 m/s at $P = 4.00$ mbar and an EFG profile yielding $E_p = 50 \text{ V} \cdot \text{cm}^{-1}$ are assumed. Ions are confined radially by a 200 V_{*p-p*} rf voltage (850 kHz) that is superimposed on the quadrupolar lens elements

electric field may be operated in either polarity. To transmit ions without mobility analysis, the DC field is adjusted to simply push ions towards the exit. During TIMS analysis, the EFG in combination with flowing gas is used to trap, analyze, and elute the ions in accordance with their mobilities. Importantly, the DC axial field has essentially no radial component in the analytically important volume of the TIMS tunnel.

Sample Preparation

To verify the theory presented below, low concentration ESI tuning mix (Agilent Technology, Santa Clara, Ca, USA) was directly infused at $\sim 180 \mu\text{L/h}$ using an electrospray ionization source. Nitrogen nebulizer gas was provided inside the sealed ionization chamber at a flow rate of 4 L/min.

Ion Trajectory Simulations

A SIMION (ver. 8.0; Ringoes, NJ, USA) model was constructed using the *collision_hs1.lua* user program to study ion dynamics inside the TIMS tunnel. The simulated tunnel was comprised of 100 individual electrodes (25 axial segments partitioned into four quadrants). Alternating voltages are applied to the electrodes to generate a quadrupolar radial field

while an axial EFG profile was superimposed on the axial segments.

Theory

General Principles of Operation

A condensed list of key terms and variables relevant to the discussion of TIMS theory is contained in Table 1. TIMS has parallels to drift tube IMS (separation based on dragging ions through a gas with a DC electric field), the aforementioned IMS experiments by Ivory, Smith, Baykut, and Loboda (utilization of gas flow and electrodynamic axial fields), as well as numerous IMS approaches that radially confine the ion swarm during separation. As demonstrated in Figure 1c, the superimposed rf voltages inhibit radial diffusion and Coulomb expansion ensuring high ion transmission. Though ion confinement is dependent on the magnitude of the pseudopotential for each m/z species [56], radial motion is independent of the time of elution and the separation performance is not significantly affected. We, therefore, restrict the subsequent discussion to the axial dimension.

As shown in Figure 1b, TIMS analysis begins by accumulating ions for a fixed period of time. During accumulation, the deflection plate is set to a repulsive potential that directs ions

Table 1. List of Key Terms and Variables

EFG	electric field gradient; the complete EFG profile includes the rising edge, plateau, and falling edge
E_p	strength of the position-independent electric field on the EFG plateau
E_0	strength of the electric field on the EFG plateau during the accumulation and trap steps and at the beginning of the elution step
E_e	strength of the electric field on the EFG plateau at the time of ion elution
L_r	axial length of the EFG rising edge
L_p	axial length of the EFG plateau
L_f	axial length of the EFG falling edge
t_e	time of ion elution; time elapsed from the start of the EFG scan (t_0) to the time the ion begins to travel across the plateau
t_f	time elapsed during ion transit across the EFG falling edge
t_p	time elapsed during ion transit across the EFG plateau
t_t	total time elapsed from the start of the EFG scan to the time when ions traverse the EFG falling edge and exit the analyzer
v_g	velocity of the buffer gas through the tunnel
V_t	instantaneous voltage across the tunnel when ions of a given K are detected
V_e	elution voltage; instantaneous voltage across the tunnel at the time of ion elution
β	rate at which the strength of the field on the EFG plateau (E_p) is scanned

into the entrance funnel. Ions pass through the entrance funnel, enter the analyzer, and traverse the EFG profile until ultimately residing at an equilibrium position along the EFG rising edge where the net force acting upon the ions is zero. Gas is directed through the tunnel by restricting flow through the port across from the capillary exit. Restricting the gas flow at this port increases the pressure across and the gas velocity through the tunnel. Ions reach their equilibrium position in the tunnel when the drift velocity of the ions through the gas is equal and opposite to the velocity of the buffer gas, v_g ,

$$v_d + v_g = 0 \quad (2)$$

Since v_d scales linearly with K by Equation 1, ions of lower K are trapped at positions further up the repulsive rising edge of the EFG profile (where the magnitude of E is larger) such that Equation 2 is satisfied. Conversely, ions of higher K are confined to positions near the entrance of the tunnel as demonstrated in Figure 1c. In the second analysis step, additional ions are prevented from entering the entrance funnel/tunnel regions by pulsing the potential of the deflector lens to an attractive potential. Ions coming from the capillary exit collide with the deflection plate and are thereby neutralized. During this time, ions residing inside the tunnel are trapped for a user-defined time period. Typically, the trap time is on the order of a few ms; however, trap times up to a few s may be employed for kinetic studies [50, 57]. In the third step, the magnitude of the EFG profile is decreased from an initial value, E_0 , at a user-defined rate such that ions of progressively higher K elute from the analyzer. The conceptual understanding of TIMS is greatly enhanced by deriving a quantitative theory that clarifies the relationship of separation performance with instrument properties and user-defined variables.

Time of Elution

In three dimensions, the flux of ions in a fluid medium under the influence of a concentration gradient, $\nabla c(r,z,t)$, gas flow, v_g , and electric field, $E(r,z,t)$, at a given time, t , is described by the Nernst-Planck equation [4]

$$\frac{\partial}{\partial t} c(r,z,t) + \nabla \cdot (-D \cdot \nabla c(r,z,t) + (v_g - K E(r,z,t)) \cdot c(r,z,t)) = 0 \quad (3)$$

Based upon the Knudsen number (Kn, the ratio of the mean free path to the dimensions of the analyzer), TIMS operates within the continuous flow regime (Kn < 0.01) such that individual ion-neutral collisional dynamics can be treated with macroscopic fluid properties including diffusion, $D \cdot \nabla c(r,z,t)$, and convection, $(v_g - K E(r,z,t)) \cdot c(r,z,t)$. Because the master equation (Equation 3) is difficult, if not impossible, to solve, our one-dimensional analytical solution relies upon breaking the experiment down into three steps: (1) the time of elution (i.e., the time from the start of the EFG scan to the time when ions begin to traverse the plateau), (2) the transit time across the plateau, and (3) the transit time across the falling edge (see Figure 1b). The relationships most relevant to the major outcomes are presented here, whereas comprehensive derivation of all expressions can be found in the [Supporting Information](#).

As shown in Figure 1c, during the accumulation and trapping steps, ions are dispersed according to their mobility along the rising edge of the EFG when,

$$E_p > v_g / K \quad (4)$$

where E_p is the magnitude of the EFG plateau. During the elution step, the EFG profile is scanned such that E_p is progressively decreased according to,

$$E_p(t) = E_0 - \beta t \quad (5)$$

where β is the time-dependent rate of change of the electric field on the plateau. At present, only linear scan functions have been employed, though nonlinear functions are also possible. The time at which ions begin to traverse the plateau (time of elution, t_e) is given by

$$t_e = \frac{E_0 - E_e}{\beta} \quad (6)$$

where E_e is the electric field strength on the plateau at the time of elution. At the time of elution, the axial forces acting upon the ions are equivalent (as described by Equation 2) such that

$$E_e = v_g / K \quad (7)$$

Substituting Equation 7 into Equation 6 yields,

$$t_e = \frac{E_0 - v_g/K}{\beta} \quad (8)$$

The time required for ions to traverse the plateau, t_p , is given by

$$t_p = \sqrt{\frac{2 L_p}{K \beta}} \quad (9)$$

where L_p is the length of the plateau. Moreover, the time required for ions to traverse the falling edge, t_f , is given by

$$t_f = \ln\left(\frac{v_g}{\sqrt{2 K \beta L_p}}\right) \cdot \frac{L_f}{v_g - \sqrt{2 K \beta L_p}} \quad (10)$$

where L_f is the length of the falling edge. The total transit time is given by summation of Equations 8, 9, and 10,

$$t_t = t_e + t_p + t_f \quad (11)$$

$$t_t = \frac{E_0 - v_g/K}{\beta} + \sqrt{\frac{2 L_p}{K \beta}} + \ln\left(\frac{v_g}{\sqrt{2 K \beta L_p}}\right) \cdot \frac{L_f}{v_g - \sqrt{2 K \beta L_p}} \quad (12)$$

Notice, the first term in Equation 12 is proportional to $1/K$, whereas the second term and third terms contain nonlinear dependence on K . As demonstrated below, the contribution of the first term is dominant.

Resolving Power

All analytical separations are characterized by their ability to differentiate two closely spaced signals. In IMS, resolving power (R) has emerged as the customary performance characteristic

$$R = \frac{K}{\Delta K} \quad (13)$$

which may alternatively be written as

$$R = \frac{K \cdot \left(\frac{dt}{dK}\right)}{\text{FWHM}_t} \quad (14)$$

where FWHM_t is the temporal width of the ion distribution. In the case of TIMS, because $t_e + t_p \gg t_f$ the transit

time across the falling edge of the EFG is neglected and Equation 12 becomes

$$t_t \approx \frac{E_0 - v_g/K}{\beta} + \sqrt{\frac{2 L_p}{K \beta}} \quad (15)$$

where the derivative function with respect to K is

$$\frac{dt_t}{dK} = \frac{v_g}{\beta K^2} - \sqrt{\frac{L_p}{\beta}} \cdot \frac{1}{\sqrt{2} K^{3/2}} \quad (16)$$

The temporal width of the ion distribution is given by

$$\text{FWHM}_t = \frac{\sqrt{\frac{16 \ln 2 k_b T K}{q} \cdot \left(\frac{L_r}{2 v_g} + \sqrt{\frac{2 L_p}{K \beta}}\right)}}{K \beta \sqrt{\frac{2 L_p}{K \beta}}} \quad (17)$$

where L_r is the length of the rising edge. Substituting Equations 16 and 17 into 14 yields the theoretical resolving power at the analyzer exit

$$R = \frac{K \beta \sqrt{\frac{2 L_p}{K \beta}} K \left(\frac{v_g}{\beta K^2} - \sqrt{\frac{L_p}{\beta}} \cdot \frac{1}{\sqrt{2} K^{3/2}}\right)}{\sqrt{\frac{16 \ln 2 k_b T K}{q} \cdot \left(\frac{L_r}{2 v_g} + \sqrt{\frac{2 L_p}{K \beta}}\right)}} \quad (18)$$

which reduces to

$$R = \frac{(v_g t_p - L_p)}{\sqrt{\frac{16 \ln 2 k_b T K}{q} \cdot \left(\frac{L_r}{2 v_g} + t_p\right)}} \quad (19)$$

via simplification and substitution of Equation 9. Under the condition that $v_g t_p \gg L_p + L_r$, Equation 19 simplifies to

$$R = \sqrt{\frac{q v_g t_p E_e}{16 \ln 2 k_b T}} \quad (20)$$

by substitution of Equation 7. In so far as the product $v_g t_p$ represents the Lagrangian path length, Equation 20 reduces further to the familiar resolving power expression for drift tube IMS [58],

$$R = \sqrt{\frac{q L E}{16 \ln 2 k_b T}} \quad (21)$$

where the product LE represents the applied potential. Note that this approximation is valid even for small values of t_p .

Because v_g is on the order of 150 m/s (see Discussion below), ion transit times across the plateau of 5 to 10 ms result in effective path lengths of roughly 75 to 150 cm, representing 15- to 30-times the physical length of the tunnel (4.6 cm), respectively. It is noteworthy that Equation 20 indicates that the majority of the analytically useful work is done on the ions as they traverse the plateau (work = force • distance = $q E_p \cdot v_g t_p$). The utility of Equation 20 is realized by substituting Equations 7 and 9 such that the dependence of key experimental variables on the resolving power is revealed,

$$R = v_g \cdot \sqrt[4]{\frac{2 L_p}{\beta}} \cdot \frac{1}{\sqrt[4]{K^3}} \cdot \sqrt{\frac{q}{16 \ln 2 k_b T}} \quad (22)$$

Equation 22 shows that resolving power in TIMS is directly proportional to v_g and $L_p^{1/4}$, and is inversely proportional to $\beta^{1/4}$ and $K^{3/4}$. Qualitatively, these relationships can be understood by considering the effect of a particular variable on the work done on the ions as they traverse the plateau. For example, increasing v_g extends the effective path length and increases the work done on the ions. Decreasing K requires an increase in the electric field strength at which the ions elute (Equation 7), thereby increasing the force on the ions and therefore the work done on them. Increasing L_p or decreasing β results in an increase in the transit time across the plateau (Equation 9), again leading to an increase in the effective path length and the work done on the ions. Moreover, the dependence of R on q and T in Equation 22 is identical to Equation 21; however, unlike Equation 21, Equation 22 contains K , meaning that the resolving power in TIMS is analyte dependent.

Results and Discussion

Time of Elution

Theoretical trends predicted from the expressions derived above were validated by extensive comparison with experimental measurements. ESI tuning mix ions were selected for these experiments because the sample contains a distribution of ions with known K_0 values in nitrogen that adopt a single conformation (or narrow distribution of conformations) in the gas phase [49]. The total transit time of ions through the TIMS analyzer was experimentally determined by subtraction of the m/z -dependent post-TIMS flight time (~ 2 to 5 ms) from the measured arrival time of ions at the TOF detector. Figure 2a and b contain plots of K_0 as a function of the instantaneous voltage across the analyzer when ions are detected (V_t) at two different pressure settings. Though the total transit time described by Equation 12 contains both linear and nonlinear dependence on K , Figure 2c and d demonstrate that the magnitude of the nonlinear terms is rather small, as t_t decreases linearly with $1/K_0$ as predicted by Equation 8. That is, the magnitude of t_p and t_f in Equation [12] is considerably smaller than t_e , as $t_e \approx t_t$ (see Figure 2e and f). Note that the dependence of t_t on K_0 in TIMS is opposite to drift tube IMS, wherein the

transit time increases (rather than decreases) linearly with $1/K$. The collective results shown in Figure 2 provide justification for calibration of the TIMS analyzer for K_0 or collision cross-section values since the transit time and V_t are linearly related through a constant β value.

Detailed inspection of the data reveals that in all cases, experimental transit times predicted by the analytical model fall between theoretical predictions for t_t and t_e . Evaluation of ions with high K_0 values ($1.01 \text{ cm}^2 \text{ V}^{-1} \text{ s}^{-1}$) at $\beta = 6920 \text{ V m}^{-1} \text{ s}^{-1}$ yields agreement of the experimental and theoretical t_t values within 1% error for all pressures investigated. However, the percent difference increases slightly for ions of lower K_0 and for the experimental conditions involving higher pressure. For example, experimental and theoretical t_t values for ions of $K_0 = 0.573 \text{ cm}^2 \text{ V}^{-1} \text{ s}^{-1}$ differ by 4% at $P = 2.9$ mbar and up to 13% at $P = 3.1$ mbar (Figure 2 e and f) because the magnitude of t_t is comparatively small (≤ 60 ms for all values of β at 3.1 mbar). Differences between experimental and theoretical transit times are likely attributed to effects from gas dynamics that are not comprehensively accounted for in the present model. That is, though v_g is treated as a constant herein, gas expansion near the exit of the tunnel would induce a decrease in both P and T , and result in a concomitant increase in v_g . Such an outcome would result in an increase in K ; however, the term $(P \cdot v_g / T)$, which is proportional to the mass flow through the tunnel, would remain constant such that the net drag force on the ions also remains constant. Therefore, it is unlikely that changes in v_g are responsible for the small differences in experimental and theoretical t_t values, but rather that the current methodology used to determine v_g slightly underestimate its magnitude. Based upon an extrapolated E_e value for ions of a particular mobility and the entrance funnel pressure, the gas velocities determined by solving by Equation 7 were ~ 160 and 180 m/s, for $P_{ent} = 2.9$ and 3.1 mbar, respectively. These values, representing roughly one-half the speed of sound, are reasonable considering the geometry of the analyzer and the pumping speed. However, we note that very small differences in the magnitude of v_g (~ 1 m/s) shift the theoretical value for t_t by a few ms, making ions with relatively short t_t values (i.e., ions having low K_0 values) more susceptible to extrapolation error. Though the present level of theory and experimental methodology are reasonably adequate at predicting the transit time, future computational fluid dynamics for determination of v_g values may improve the overall accuracy.

Resolving Power

Figure 3 shows a comparison of theoretically and experimentally measured resolving power values as a function of the EFG scan rate at two different pressures. Experimental measurements are in excellent qualitative agreement with theoretical predictions in that R scales linearly with $\sqrt[4]{1/\beta}$ as predicted by Equation 22. In each case, the correlation coefficients for the line of best fit were $R^2 \geq 0.99$. It is noteworthy that the dependence of R on $\sqrt[4]{1/\beta}$ is consistent with observations in the

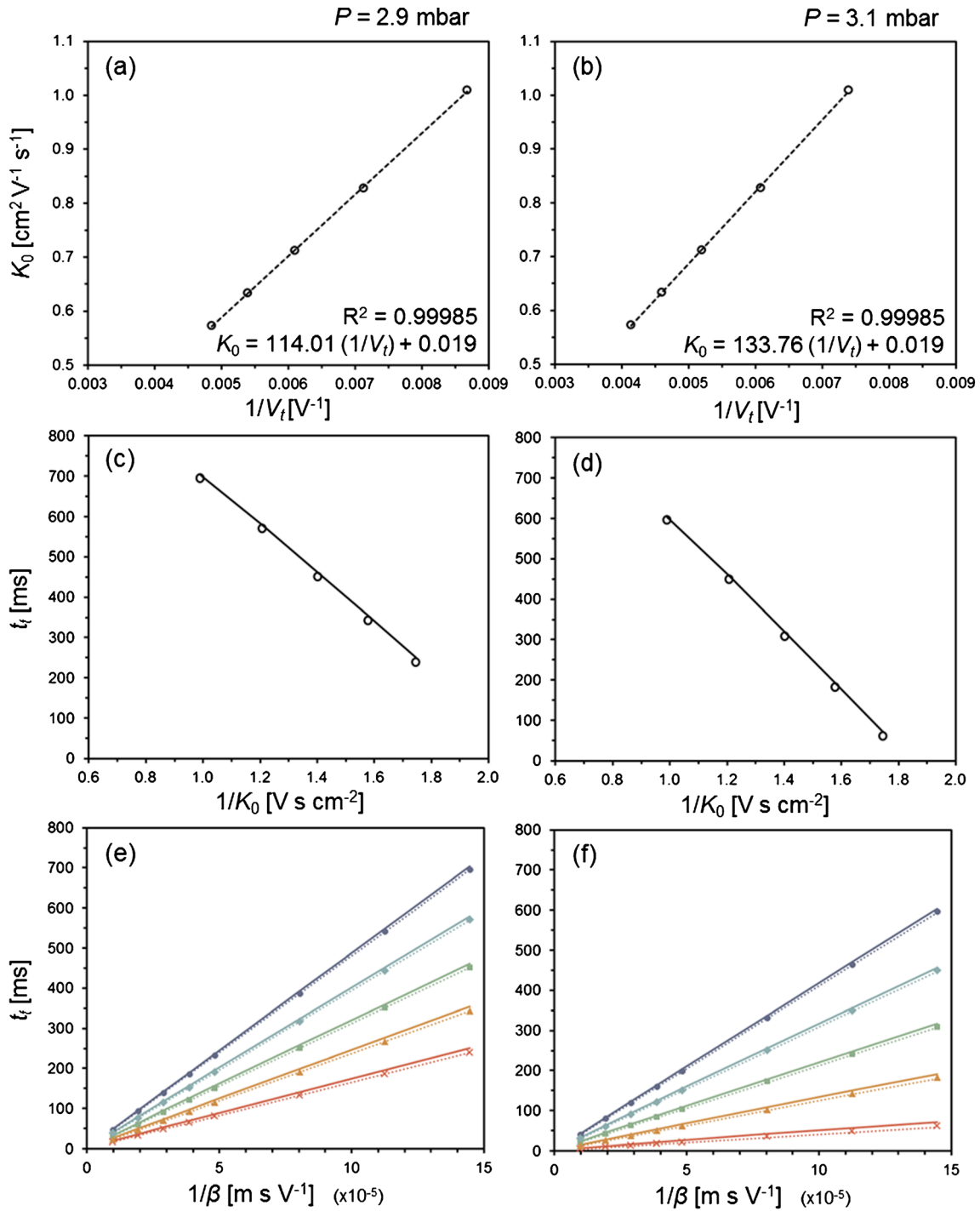


Figure 2. Parameters governing the transit time of ions in a TIMS experiment shown at two experimental pressure settings. For all plots, solid lines represent theoretical trends from Equation 12, experimental values are shown with representative symbols, and dashed lines represent best-fit linear regression functions of the experimental data. In (a) and (b), K_0 is plotted against $1/V_t$, whereas in (c) and (d) t_t is plotted against $1/K_0$ for constant $\beta = 6920$ V m⁻¹ s⁻¹. In (e) and (f), t_t is plotted against $1/\beta$ for each species (\bullet $K_0 = 1.01$, \blacklozenge 0.828, \blacksquare 0.713, \blacktriangle 0.633, and \times 0.573 cm² V⁻¹ s⁻¹). Note that the dotted line represents t_{e^+} , shown for comparison

literature [5]. As one might expect for a hybrid IM-MS platform, experimental values are lower than the theoretical predictions by roughly 15% to 30%—an effect that is attributable to several factors including (1) curvature of the axial electric

field at the edges of the plateau leading to a smaller effective path length, (2) radial asymmetry in the gas flow through the tunnel, and (3) peak broadening of the ion swarm en route to the TOF detector. Figure 3 and the TIMS distribution shown in

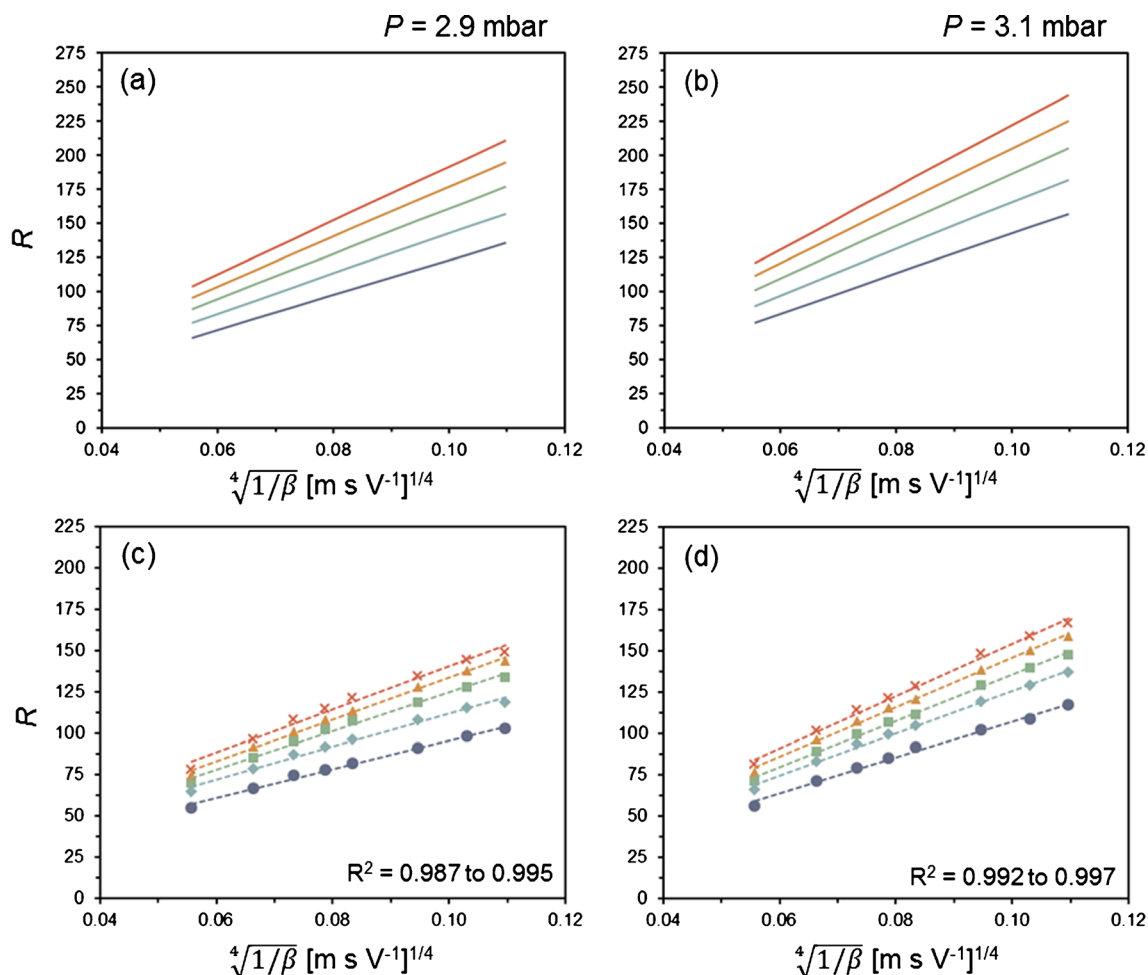


Figure 3. Resolving power trends as a function of β shown at two experimental pressure settings. For all plots, solid lines represent theoretical trends from Equation 19, experimental values are shown with representative symbols, and dashed lines represent best-fit linear regression functions of the experimental data. R is plotted against $\sqrt[4]{1/\beta}$ yielding a linear relationship for theoretical (a) and (b), and experimental (c) and (d) data for each ion species (see Figure 2 caption for legend)

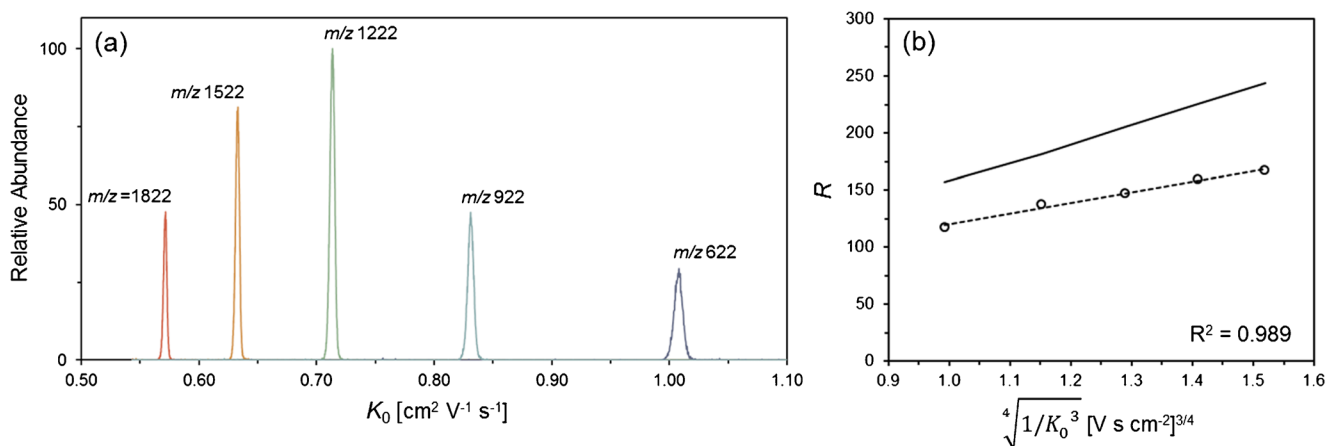


Figure 4. (a) Experimental separation of ESI tuning mix ions m/z 622 to 1822 at 3.1 mbar and constant $\beta = 6920 \text{ V m}^{-1} \text{ s}^{-1}$. Measured V_r values were converted to K_0 values using the expression listed in Figure 2 (b). (b) Resolving power as a function of K_0 : the solid line represents the theoretical trend from Equation 19, experimental values are shown with open circles, and the dashed line represents the best-fit linear regression function of the experimental data

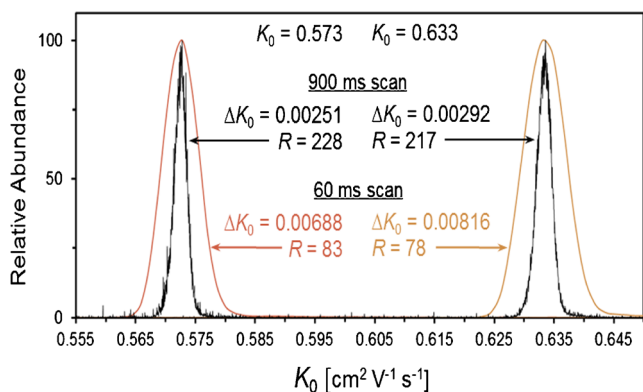


Figure 5. Mobiligram of $K_0 = 0.633$ and $0.573 \text{ cm}^2 \text{ V}^{-1} \text{ s}^{-1}$ acquired at 3.6 mbar and $\beta = 2691 \text{ V m}^{-1} \text{ s}^{-1}$ (900 ms scan time, black trace). For comparison, a mobiligram acquired at 3.1 mbar and $\beta = 103,800 \text{ V m}^{-1} \text{ s}^{-1}$ (60 ms scan time, red, and orange traces) is also shown

Figure 4a also indicate that contrary to drift tube IMS, resolving power in TIMS is analyte dependent since R increases for ions of lower K . To confirm the $\sqrt[4]{1/K^3}$ dependence predicted by Equation 22, experimental data was plotted as a function of K_0 for constant β (see Figure 4b). Experimental and theoretical trends are in agreement ($R^2 = 0.989$) and similar results were also observed at other pressure settings and values of β .

Thus far, experimental measurements have validated the dependence of β and K on the resolving power. The effect of varying the plateau length, L_p , was not experimentally verified here, but may be included in future work. Trends related to ion charge state and buffer gas temperature were also not investigated, but their dependence is predicted to be identical to that of drift tube IMS instruments [1]. Though detailed effects related to v_g were not investigated formally, the results presented here collectively demonstrate that superior resolving power is attained for experimental conditions involving higher pressure in the entrance funnel. This result is due to an increase in the magnitude of v_g and subsequent increase in E_e as well as a decrease in K . The previously discussed results shown in Figure 3 suggest that resolving power can be maximized for ions of low K_0 by increasing the pressure and minimizing β . To experimentally validate these concepts, a leak valve was installed in the entrance funnel chamber to add additional N_2 gas, such that the pressure in the entrance funnel was increased to 3.6 mbar. Next, β was minimized by (1) adjusting the magnitude of the EFG, such that only $K_0 = 0.633$ and $0.573 \text{ cm}^2 \text{ V}^{-1} \text{ s}^{-1}$ were trapped and eluted from the analyzer, and (2) maximizing the scan time. The mobiligram, shown in Figure 5, demonstrates that under these conditions, resolving power exceeding 220 is attained for singly charged ions. Based upon Equation 22 and the collective experimental results discussed herein, this work has demonstrated high performance capabilities currently

offered by TIMS, and identified key variables for future design improvement.

Conclusions

A one-dimensional analytical model for TIMS has been derived and experimentally validated. The model provides quantitative predictions for ion transit times and resolving power based on fundamental variables such as the ion mobility coefficient, EFG scan rate, and gas velocity. The linear dependence of the transit time with $1/K$ provides a fundamental basis for calibration of TIMS for either reduced mobility or collision cross-section values. The resolving power equation for TIMS reduces to a form identical to that used in drift tube IMS. Equation 20 indicates that the vast majority of the analytically meaningful work is done on the ions as they traverse the EFG plateau. The experimentally measured dependence of resolving power on the ion's mobility and the EFG scan rate was in excellent agreement with theory. According to theory, TIMS resolving power is linearly dependent on gas velocity, v_g , (Equation 22), offering a straightforward path for further improvement of TIMS performance.

Acknowledgments

The authors thank Nathan Park for his assistance in the laboratory.

References

1. Revercomb, H.E., Mason, E.A.: Theory of plasma chromatography/gaseous electrophoresis. *Rev. Anal. Chem.* **47**, 970–983 (1975)
2. Mason, E.A., McDaniel, E.W.: *Transport Properties of Ions in Gases*. John Wiley and Sons, New York (1988)
3. Zeleny, J.: On the ratio of the velocities of the two ions produced in gases by Rontgen radiation; and on some related phenomena. *Philos. Mag.* **46**, 120–154 (1898)
4. Huang, Z., Ivory, C.F.: Digitally controlled electrophoretic focusing. *Anal. Chem.* **71**, 1628–1632 (1999)
5. Loboda, A.: Novel ion mobility setup combined with collision cell and time-of-flight mass spectrometer. *J. Am. Soc. Mass Spectrom.* **17**, 691–699 (2006)
6. Gidden, J., Bowers, M., Jackson, A., Scrivens, J.: Gas-phase conformations of cationized poly(styrene) oligomers. *J. Am. Soc. Mass Spectrom.* **13**, 499–505 (2002)
7. Trimpin, S., Clemmer, D.E.: Ion mobility spectrometry/mass spectrometry snapshots for assessing the molecular compositions of complex polymeric systems. *Anal. Chem.* **80**, 9073–9083 (2008)
8. Brocker, E.R., Anderson, S.E., Northrop, B.H., Stang, P.J., Bowers, M.T.: Structures of metallosupramolecular coordination assemblies can be obtained by ion mobility spectrometry mass spectrometry. *J. Am. Chem. Soc.* **132**, 13486–13494 (2010)
9. Hoskins, J.N., Trimpin, S., Grayson, S.M.: Architectural differentiation of linear and cyclic polymeric isomers by ion mobility spectrometry mass spectrometry. *Macromolecules.* **44**, 6915–6918 (2011)
10. Forsythe, J.G., Stow, S.M., Nefzger, H., Kwiecien, N.W., May, J.C., McLean, J.A., Hercules, D.M.: Structural characterization of methylenedianiline regioisomers by ion mobility mass spectrometry, tandem mass spectrometry, and computational strategies. I. Electrospray spectra of 2-ring isomers. *Anal. Chem.* **86**, 4362–4370 (2014)

11. von Helden, G., Gotts, N.G., Bowers, M.T.: Experimental evidence for the formation of fullerenes by collisional heating of carbon rings in the gas phase. *Nature*. **363**, 60–63 (1993)
12. Hunter, J.M., Fye, J.L., Jarrold, M.F., Bower, J.E.: Structural transitions in size-selected germanium cluster ions. *Phys. Rev. Lett.* **73**, 2063–2066 (1994)
13. Clemmer, D.E., Shelimov, K.B., Jarrold, M.F.: Gas-phase self-assembly of endohedral metallofullerenes. *Nature*. **367**, 718–720 (1994)
14. von Helden, G., Wyttenbach, T., Bowers, M.T.: Conformation of macromolecules in the gas phase: use of matrix-assisted laser desorption methods in ion chromatography. *Science*. **267**, 1483–1485 (1995)
15. Servage, K.A., Silveira, J.A., Fort, K.L., Russell, D.H.: Evolution of hydrogen bond networks in protonated water clusters $H^+(H_2O)_n$ ($n = 1$ to 120) studied by cryogenic ion mobility mass spectrometry. *J. Phys. Chem. Lett.* **11**, 1825–1830 (2014)
16. Clemmer, D.E., Hudgins, R.R., Jarrold, M.F.: Naked protein conformations: cytochrome *c* in the gas phase. *J. Am. Chem. Soc.* **117**, 10141–10142 (1995)
17. Ruotolo, B.T., Giles, K., Campuzano, I., Sandercock, A.M., Bateman, R.H., Robinson, C.V.: Evidence for macromolecular protein rings in the absence of bulk water. *Science*. **310**, 1658–1661 (2005)
18. Bernstein, S.L., Dupuis, N.F., Lazo, N.D., Wyttenbach, T., Condron, M.M., Bitan, G., Teplow, D.B., Shea, J.E., Ruotolo, B.T., Robinson, C.V., Bowers, M.T.: Amyloid- β protein oligomerization and the importance of tetramers and dodecamers in the aetiology of Alzheimer's disease. *Nat. Chem.* **1**, 326–331 (2009)
19. Pierson, N.A., Chen, L., Valentine, S.J., Russell, D.H., Clemmer, D.E.: Number of solution states of bradykinin from ion mobility and mass spectrometry measurements. *J. Am. Chem. Soc.* **133**, 13810–13813 (2011)
20. Bleiholder, C., Dupuis, N.F., Wyttenbach, T., Bowers, M.T.: Ion mobility-mass spectrometry reveals a conformational conversion from random assembly to β -sheet in amyloid fibril formation. *Nat. Chem.* **3**, 172–177 (2011)
21. Uetrecht, C., Barbu, I.M., Shoemaker, G.K., van Duijn, E., Heck, A.J.R.: Interrogating viral capsid assembly with ion mobility-mass spectrometry. *Nat. Chem.* **3**, 126–132 (2011)
22. Hall, Z., Politis, A., Bush, M.F., Smith, L.J., Robinson, C.V.: Charge-state dependent compaction and dissociation of protein complexes: insights from ion mobility and molecular dynamics. *J. Am. Chem. Soc.* **134**, 3429–3438 (2012)
23. Papadopoulos, G., Svendsen, A., Boyarkin, O., Rizzo, T.: Conformational distribution of bradykinin $[bk+2H]^{2+}$ revealed by cold ion spectroscopy coupled with FAIMS. *J. Am. Soc. Mass Spectrom.* **23**, 1173–1181 (2012)
24. Politis, A., Park, A.Y., Hall, Z., Ruotolo, B.T., Robinson, C.V.: Integrative modeling coupled with ion mobility mass spectrometry reveals structural features of the clamp loader in complex with single-stranded DNA binding protein. *J. Mol. Biol.* **425**, 4790–4801 (2013)
25. Hines, K.M., Ashfaq, S., Davidson, J.M., Opalenik, S.R., Wikswo, J.P., McLean, J.A.: Biomolecular signatures of diabetic wound healing by structural mass spectrometry. *Anal. Chem.* **85**, 3651–3659 (2013)
26. Allen, S.J., Schwartz, A.M., Bush, M.F.: Effects of polarity on the structures and charge states of native-like proteins and protein complexes in the gas phase. *Anal. Chem.* **85**, 12055–12061 (2013)
27. Chen, L., Chen, S.H., Russell, D.H.: An experimental study of the solvent-dependent self-assembly/disassembly and conformer preferences of gramicidin A. *Anal. Chem.* **85**, 7826–7833 (2013)
28. Pierson, N.A., Chen, L., Russell, D.H., Clemmer, D.E.: Cis-trans isomerizations of proline residues are key to bradykinin conformations. *J. Am. Chem. Soc.* **135**, 3186–3192 (2013)
29. Silveira, J.A., Fort, K.L., Kim, D., Servage, K.A., Pierson, N.A., Clemmer, D.E., Russell, D.H.: From solution to the gas phase: stepwise dehydration and kinetic trapping of Substance P reveals the origin of peptide conformations. *J. Am. Chem. Soc.* **135**, 19147–19153 (2013)
30. Bleiholder, C., Do, T.D., Wu, C., Economou, N.J., Bernstein, S.S., Buratto, S.K., Shea, J.E., Bowers, M.T.: Ion mobility spectrometry reveals the mechanism of amyloid formation of A β and its modulation by inhibitors at the molecular level: epigallocatechin gallate and scyllo-inositol. *J. Am. Chem. Soc.* **135**, 16926–16937 (2013)
31. Schenk, E.R., Mendez, V., Landrum, J.T., Ridgeway, M.E., Park, M.A., Fernandez-Lima, F.: Direct observation of differences of carotenoid polyene chain cis/trans isomers resulting from structural topology. *Anal. Chem.* **86**, 2019–2024 (2014)
32. Wyttenbach, T., von Helden, G., Batka, J., Carlat, D., Bowers, M.T.: Effect of the long-range potential on ion mobility measurements. *J. Am. Soc. Mass Spectrom.* **8**, 275–282 (1997)
33. May, J., Russell, D.: A mass-selective variable-temperature drift tube ion mobility-mass spectrometer for temperature dependent ion mobility studies. *J. Am. Soc. Mass Spectrom.* **22**, 1134–1145 (2011)
34. Silveira, J.A., Servage, K.A., Gamage, C.M., Russell, D.H.: Cryogenic ion mobility-mass spectrometry captures hydrated ions produced during electrospray ionization. *J. Phys. Chem. A*. **117**, 953–961 (2013)
35. Giles, K., Pringle, S.D., Worthington, K.R., Little, D., Wildgoose, J.L., Bateman, R.H.: Applications of a traveling wave-based radio-frequency-only stacked ring ion guide. *Rapid. Commun. Mass Spectrom.* **18**, 2401–2414 (2004)
36. Gillig, K.J., Ruotolo, B.T., Stone, E.G., Russell, D.H.: An electrostatic focusing ion guide for ion mobility-mass spectrometry. *Int. J. Mass Spectrom.* **239**, 43–49 (2004)
37. Bush, M.F., Hall, Z., Giles, K., Hoyes, J., Robinson, C.V., Ruotolo, B.T.: Collision cross sections of proteins and their complexes: a calibration framework and database for gas-phase structural biology. *Anal. Chem.* **82**, 9557–9565 (2010)
38. Blase, R.C., Silveira, J.A., Gillig, K.J., Gamage, C.M., Russell, D.H.: Increased ion transmission in IMS: a high resolution, periodic-focusing DC ion guide ion mobility spectrometer. *Int. J. Mass Spectrom.* **301**, 166–173 (2011)
39. Shaffer, S.A., Tang, K., Anderson, G.A., Prior, D.C., Udseth, H.R., Smith, R.D.: A novel ion funnel for focusing ions at elevated pressure using electrospray ionization mass spectrometry. *Rapid. Commun. Mass Spectrom.* **11**, 1813–1817 (1997)
40. Shaffer, S.A., Prior, D.C., Anderson, G.A., Udseth, H.R., Smith, R.D.: An ion funnel interface for improved ion focusing and sensitivity using electrospray ionization mass spectrometry. *Anal. Chem.* **70**, 4111–4119 (1998)
41. Koeniger, S.L., Merenbloom, S.I., Valentine, S.J., Jarrold, M.F., Udseth, H.R., Smith, R.D., Clemmer, D.E.: An IMS-IMS analogue of MS-MS. *Anal. Chem.* **78**, 4161–4174 (2006)
42. Baker, E.S., Clowers, B.H., Li, F., Tang, K., Tolmachev, A.V., Prior, D.C., Belov, M.E., Smith, R.D.: Ion mobility spectrometry-mass spectrometry performance using electrodynamic ion funnels and elevated drift gas pressures. *J. Am. Soc. Mass Spectrom.* **18**, 1176–1187 (2007)
43. Kemper, P.R., Dupuis, N.F., Bowers, M.T.: A new, higher resolution ion mobility mass spectrometer. *Int. J. Mass Spectrom.* **287**, 46–57 (2009)
44. Kelly, R.T., Tolmachev, A.V., Page, J.S., Tang, K., Smith, R.D.: The ion funnel: theory, implementations, and applications. *Mass Spectrom. Rev.* **29**, 294–312 (2010)
45. Fort, K.L., Silveira, J.A., Russell, D.H.: The periodic focusing ion funnel: theory, design, and experimental characterization by high-resolution ion mobility-mass spectrometry. *Anal. Chem.* **85**, 9543–9548 (2013)
46. May, J.C., Goodwin, C.R., Lareau, N.M., Leaprot, K.L., Morris, C.B., Kurulugama, R.T., Mordehai, A., Klein, C., Barry, W., Darland, E.: Conformational ordering of biomolecules in the gas phase: nitrogen collision cross sections measured on a prototype high resolution drift tube ion mobility mass spectrometer. *Anal. Chem.* **86**, 2107–2116 (2014)
47. Page, J.S., Tolmachev, A.V., Tang, K., Smith, R.D.: Variable low-mass filtering using an electrodynamic ion funnel. *J. Mass Spectrom.* **40**, 1215–1222 (2005)
48. Baykut, G., von Halem, O., Raether, O.: Applying a dynamic method to the measurement of ion mobility. *J. Am. Soc. Mass Spectrom.* **20**, 2070–2081 (2009)
49. Hernandez, D.R., DeBord, J.D., Ridgeway, M.E., Kaplan, D.A., Park, M.A., Fernandez-Lima, F.: Ion dynamics in a trapped ion mobility spectrometer. *Analyst*. **139**, 1913–1921 (2014)
50. Silveira, J.A., Ridgeway, M.E., Park, M.A.: High resolution trapped ion mobility spectrometry of peptides. *Anal. Chem.* **86**, 5624–5627 (2014)
51. Park, M.A.: Apparatus and method for parallel flow ion mobility spectrometry combined with mass spectrometry. US Patent 8,288,717 (2012)
52. Fernandez-Lima, F., Kaplan, D.A., Park, M.A.: Integration of trapped ion mobility spectrometry with mass spectrometry. *Rev. Sci. Instrum.* **82**, 126106 (2011)
53. Fernandez-Lima, F., Kaplan, D., Suetering, J., Park, M.: Gas-phase separation using a trapped ion mobility spectrometer. *Int. J. Ion. Mobil. Spectrom.* **14**, 93–98 (2011)
54. Park, M.A., Kim, T., Stacey, C., Berg, C.: Ion guide for mass spectrometers. US Patent 7,459,693 (2008)

55. Park, M.A.: US Patent Apparatus and method for parallel flow ion mobility spectrometry combined with mass spectrometry. US Patent 7,838,826 (2010)
56. Gerlich, D.: Inhomogeneous rf fields: a versatile tool for the study of processes with slow ions. John Wiley and Sons, Malden, MA (1992)
57. Schenk, E.R., Ridgeway, M.E., Park, M.A., Leng, F., Fernandez-Lima, F.: Isomerization kinetics of AT hook decapeptide solution structures. *Anal. Chem.* **86**, 1210–1214 (2013)
58. Rokushika, S., Hatano, H., Baim, M.A., Hill, H.H.: Resolution measurement for ion mobility spectrometry. *Anal. Chem.* **57**, 1902–1907 (1985)